A Validation of a Satellite Cloud Retrieval during ASTEX

S. PLATNICK*

NASA Ames Research Center, Moffett Field, California

FRANCISCO P. J. VALERO

California Space Institute, Scripps Institution of Oceanography, University of California, San Diego, La Jolla, California

(Manuscript received in final form 16 June 1994)

ABSTRACT

An algorithm using *NOAA-12* AVHRR (Advanced Very High Resolution Radiometer) solar reflectance measurements for retrieving cloud droplet size and optical thickness has been applied to a boundary layer stratocumulus cloud in the vicinity of the Azores on 12 June 1992 during the Atlantic Stratocumulus Transition Experiment (ASTEX). This day was particularly advantageous for validations because of the absence of cirrus or other higher-level clouds during the satellite overpass and the existence of a large relatively uniform stratus cloud deck. Uncertainty estimates for the retrievals are presented along with a discussion of the algorithm. An in-flight absolute calibration of AVHRR channel 1, necessary for accurate optical thickness retrievals, was done concurrently with the retrievals through comparison with a visible radiometer flown on the National Aeronautics and Space Administration's ER-2 and using the stratus cloud as the common reflectance target. Results are compared with in situ microphysical measurements taken with the Particulate Volume Monitor (PVM-100) and Forward Scattering Spectrometer Probe (FSSP-100) instruments on the University of Washington C-131A aircraft. Satellite retrievals of both optical thickness and droplet size lie within the values measured by the two in situ instruments.

1. Introduction

Clouds have long been recognized as a key modifier of climate but, with their spatial and temporal variability, they are among the most difficult components of the climate system to study. There is significant disagreement in estimates of present-day cloud radiative forcing. Further, possible modifications to climate from changing cloud parameters, or cloud sensitivities, are not well understood (Cess et al. 1990; Arking 1991). Two important cloud parameters needed for understanding the radiative role of clouds on climate are optical thickness and droplet size (e.g., Slingo 1989; Fouquart et al. 1990; Twomey 1974, 1991). Satellite remote sensing techniques are needed for a global knowledge of these two parameters.

Cloud optical thickness and droplet size can be inferred from solar reflection measurements at absorbing and nonabsorbing wavelengths for water (Hansen and Pollack 1970). Reflectance at nonabsorbing wavelengths, applicable throughout the visible, contains information primarily regarding optical thickness. Cloud droplet absorption becomes significant at wavelengths into the near infrared and is approximately proportional to droplet radius; consequently, cloud reflectance measurements at absorbing wavelengths contain information about droplet size. Wavelengths with the greater water absorption give reflectances with less dependence on optical thickness and thereby generally a less ambiguous inference of droplet size. Practical choices for near-infrared wavelengths are limited to atmospheric windows where above-cloud transmission is relatively large. Measurements of cloud reflectance and subsequent retrievals of optical thickness and droplet size have been made by a number of investigators. Studies making use primarily of the 1.6- and/or 2.2-μm atmospheric windows include the aircraft investigations of Twomey and Cocks (1982, 1989), Foot (1988), Rawlins and Foot (1990), Nakajima and King (1990), and Nakajima et al. (1991), and the Skylab study of Curran and Wu (1982).

While cloud reflectance in the 3.7-μm window is ideal for determining droplet size because of its greater water absorption compared with shorter wavelengths (an order of magnitude greater absorption than at 2.2 μm), its use is complicated because emission at this wavelength, for typical droplet sizes encountered, is comparable to the reflected radiance. However, a steady interest in this band has been developing, in no

* Current affiliation: NASA Goddard Space Flight Center, Greenbelt, Maryland.

Corresponding author address: Dr. S. Platnick, Code 913, NASA GSFC, Greenbelt, MD 20771.

© 1995 American Meteorological Society

small part due to the long-time availability of a 3.7-μm channel on the Advanced Very High Resolution Radiometer (AVHRR) instrument onboard the National Oceanic and Atmospheric Administration (NOAA) polar-orbiting satellites. Quantitative cloud retrievals using the AVHRR were first made by Arking and Childs (1985) and more recently by Kaufman and Nakajima (1993), Platnick and Twomey (1994), and Han et al. (1994). Other satellite instruments using the 3.7-μm band include the recently launched *GOES-8* and the future Earth Observing System's Moderate Resolution Imaging Spectroradiometer (MODIS) instrument (King et al. 1992).

Retrievals of cloud droplet radius reported in the aircraft studies, which did not use a 3.7-μm channel, showed a systematic excess bias when compared with in situ measurements. The larger retrieved radii imply a larger droplet absorption than is accounted for by current theory and has been termed "anomalous absorption." For example, Twomey and Cocks (1982, 1989) reported that retrieved radii were about 5 μm larger than their in-cloud measurements. Twomey and Cocks analyzed possible reasons for the difference including excess absorption of both liquid water and water vapor, and holes or other variability in cloud optical thickness. No reasonable explanation was found that could account for the discrepancy. An overestimate of droplet radius by 2–3 μm was reported by both Rawlins and Foot (1990) and Nakajima et al. (1991) compared with Forward Scattering Spectrometer Probes (FSSP) manufactured by Particle Measuring Systems, Inc. (Knollenberg 1981). Taylor (1992) reported that estimates of water vapor path absorption, both above cloud and in cloud, using the improved band models of LOWTRAN 7 reduced the discrepancy found by Rawlins and Foot, who based their water vapor corrections on LOWTRAN 5. However, this does not explain the results of Twomey and Cocks, who used an onboard calibrated solar diffuser as a reflectance reference and did not need to account for atmospheric transmittance of solar irradiance to cloud top. Further, present calculations, using a *k*-distribution technique calculated with line-by-line data and including LOWTRAN 7 continuum absorption models, show that in-cloud water vapor absorption would not account for the discrepancies seen by Twomey and Cocks. For example, interstitial vapor absorption in an optically thick, low cloud would increase retrieved radii by no more than 5% for a 2.2-μm channel and 3% for a 1.6-μm channel. A similar analysis for cloud vapor absorption has been made for the AVHRR 3.7-μm channel and is discussed in section 4 of this paper. Stephens and Tsay (1990) give a summary of anomalous cloud absorption, which is also found in broadband measurements. Whether a 3.7-μm channel droplet size retrieval would suffer from such an anomaly needs to be determined. It is likely that the large liquid water absorption in this band, and subsequently smaller number of average scatterings for reflected photons, would reduce the effect of cloud inhomogeneities and uncertainties in gaseous absorption.

Validation is especially problematic for satellite-borne sensors because of the need for in situ measurements coordinated spatially and temporally with the satellite overpass. No validation of the AVHRR retrievals, using the 3.7-μm channel, were made in the previously mentioned studies. However, some comparisons were made by Platnick and Twomey (1994) for two scenes off the coast of southern California, where in situ microphysical data were obtained during the FIRE [First ISCCP (International Satellite Cloud Climatology Project) Regional Experiment] field observations in 1987. AVHRR retrievals of optical thickness and droplet radius compared well with the cloud-top measurements reported by Rawlins and Foot (1990) but were a few micrometers larger than the midcloud measurements of Radke et al. (1989). The need for a more comprehensive validation study for the 3.7-μm band is the impetus for the current work.

The Atlantic Stratocumulus Transition Experiment (ASTEX) studied the radiative, microphysical, and dynamic properties of marine boundary layer stratocumulus clouds in the region of the Azores in June 1992 (Bluth and Albrecht 1993). During the experiment, several coordinated flights of aircraft with NOAA satellite overpasses provided an opportunity to validate AVHRR cloud retrievals. Unfortunately, many of these coordinated flights occurred when some combination of cirrus, extensive haze, or broken stratocumulus clouds were present, each by itself complicating the retrievals. None of these conditions occurred on 12 June 1992 when the University of Washington C-131A aircraft made in situ cloud microphysical measurements in uniform stratus during an overpass of *NOAA-12*. The C-131A flew two main cloud microphysical instruments. The Forward Scattering Spectrometer Probe (FSSP-100) and a new Particulate Volume Monitor (PVM-100) developed by Gerber Scientific Inc. (Gerber et al. 1994) were used to measure droplet size and cloud liquid water content. The National Aeronautics and Space Administration's (NASA) ER-2 high-altitude aircraft, equipped with a cloud lidar system (Spinhirne et al. 1989) and visible and infrared radiometers, overflew the stratus at the same time. The visible radiometer is used for an in-flight calibration of AVHRR channel 1 (0.65 μm) using the stratus cloud as the common reflectance target. Reducing the uncertainty in visible reflectance is important for accurate retrievals of optical thickness. We begin the paper with a discussion of the physics of cloud remote sensing in section 2. The retrieval algorithm is presented in section 3 followed by an uncertainty analysis in section 4. In section 5 we report *NOAA-12* AVHRR retrievals of optical thickness and droplet radius for the cloud region of 12 June 1992 and compare these retrievals with in situ measurements obtained from the C-131A using the PVM and FSSP instruments.

2. The physics of cloud remote sensing

Cloud reflectance depends primarily on the cloud's optical thickness τ, droplet single scattering albedo ϖ_0, and droplet phase function (primarily the asymmetry parameter g). In turn, each of the parameters are a function of wavelength and the droplet size distribution $n(r)$ through the wavelength-dependent complex index of refraction and droplet size parameter ($2\pi r/\lambda$). Fortunately, the exact nature of the size distribution is not critical and the radiative parameters depend largely on the effective radius r_{eff} defined as (Hansen and Travis 1974)

$$r_{\text{eff}} = \frac{\int r^3 n(r)\,dr}{\int r^2 n(r)\,dr}. \qquad (1)$$

It is assumed that the effective radius is inferred from remote sensing. We will examine this assumption in more detail in section 4. Effective radii for nonprecipitating boundary layer clouds are expected to lie within a range of about 5–20 μm.

Throughout the visible, single-scattering albedo is unity, or very nearly so, and absorption ($1 - \varpi_0$) is negligible for all droplet sizes. However, slight increases in the asymmetry parameter with effective radius, implying greater forward scattering and more difficulty in a photon being turned around, reduce reflectance. This is shown in Fig. 1a where bidirectional reflectance as a function of optical thickness and effective radius is given for AVHRR channel 1 ($\sim$0.65 μm). In this conservative scattering case, all curves approach unity with increasing optical thickness (exactly unity for the albedo). With the exception of a 1-μm radius, the effective radii curves lie near each other, indicating that a measurement in the visible contains good information regarding optical thickness. Optical thickness is a function of both wavelength and droplet size because of the size parameter dependence of the extinction efficiency, $Q_e(r/\lambda)$, since $\tau(r,\lambda) \propto \int Q_e(r/\lambda) r^2 n(r)\,dr = \overline{Q_e}(\lambda) \int r^2 n(r)\,dr$, where $\overline{Q_e}(\lambda)$ is the size-averaged extinction efficiency at some wavelength. However, it is desirable for a measured cloud to be represented by the same abscissa for all wavelengths and sizes so that comparison between different curves is simplified. This is accomplished by scaling the optical thickness by $2/\overline{Q_e}(\lambda)$, which gives a value appropriate in the visible; all references to optical thickness refer to this scaled quantity.

For AVHRR channel 3 (at 3.7 μm), droplet absorption is significant and increases with effective radius (from $1 - \varpi_0$ being about 0.04 at $r_{\text{eff}} = 4$ μm to 0.2 at 20 μm). There is less chance of a photon penetrating deep into a cloud and then back out through the cloud top without being absorbed. Eventually a cloud becomes so thick that no further increase in reflectance is possible. Figure 1b shows this asymptotic limit to reflectance for optically thick clouds; the larger the absorption, or radius, the smaller the reflectance. For optical thickness greater than about 4–7, a measured reflectance can be used to determine effective radius unambiguously. An exception is seen for the 1-μm radius curve that crosses the other curves. Its lone behavior is due to a relatively small extinction efficiency ($\approx$0.75) and would not be apparent without the optical thickness scaling previously mentioned. However, this is an unlikely droplet size for realistic clouds, and the multiple solution can be ignored. So a measurement of reflectance in the visible and 3.7-μm channel can be combined to infer both optical thickness and droplet size. The solutions are obtained by determining the best fit between the measured cloud reflectances in each

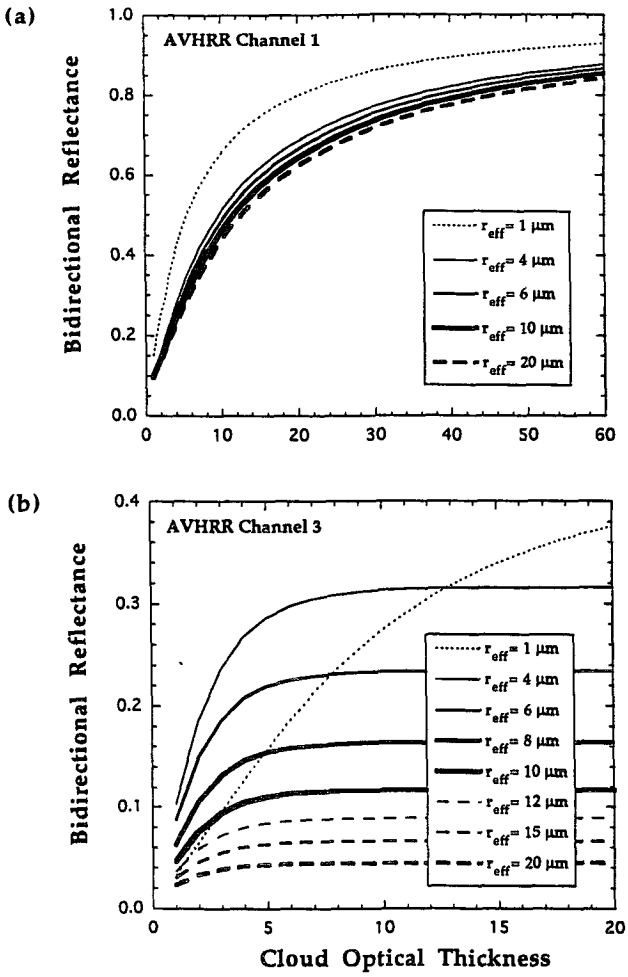

FIG. 1. Bidirectional reflectance for (a) AVHRR channel 1, and (b) AVHRR channel 3 for various effective radii r_{eff} as a function of cloud optical thickness. Calculations are for an azimuthal average with cosine of the solar and satellite viewing angles of $\mu_0 = 0.65$ and $\mu = 0.95$, respectively; an effective variance of 0.05; and *NOAA-11* spectral bandpasses. Lambertian surface albedos are 0.06 and 0.01 for channels 1 and 3, respectively.

channel and the entries in a library of reflectances calculated for a variety of effective radii and optical thicknesses, and at appropriate solar and satellite viewing angles.

Emission at terrestrial temperatures is significant for the 3.7-μm channel when compared with the solar cloud reflection component. By virtue of Kirchoff's law, cloud emissivity at any angle is equated with fractional absorption at the same angle. For the case of a thin cloud, both surface and cloud emission contribute to the total radiance seen by the satellite. In addition, if the surface reflectance is nonzero in the channel, then the combined, higher-order reflections off the cloud and surface need to be included. For example, a cloud emits radiation downward to the surface as well as upward to the satellite, and this downward emission can reflect off the surface and be transmitted through the cloud contributing to the upward signal. This calculation can be handled by a doubling or adding algorithm where the lower layer is now a water or ground surface with some specified bidirectional reflectance. Cloud-top-emitted radiance depends on both surface and cloud temperatures, which are not known a priori. To leave these temperatures as variables, a calculation of the *effective* emissivities for both the cloud and the surface are made (Figs. 2a, 2b). The effective surface emissivity is defined such that its product with the Planck function, evaluated at the surface temperature, gives the net upward radiance emerging at cloud top due to emission originating at the surface. Effective cloud emissivity is similarly defined but using the Planck radiance at the cloud's temperature. The emissivities are effective in the sense that they include the cloud's transmittance and all higher-order reflections. As an example, for a black surface at 3.7 μm, approximated by the ocean, the effective cloud emissivity becomes the actual emissivity of the cloud while the effective surface emissivity equals the cloud transmittance. For a thick cloud, effective surface emissivity goes to zero along with cloud transmittance. In this study, the cloud is considered to be at a uniform temperature. In Fig. 2a, effective cloud emissivity is seen to *increase* with droplet size, or droplet absorption, as expected. The effective emissivity of the surface in Fig. 2b *decreases* with droplet size since greater droplet absorption leads to a decrease in cloud transmittance. Note that the optical thickness where either emissivity reaches its asymptotic limit is about twice that for reflectance (Fig. 1b).

The larger the effective radius, the smaller the solar reflectance and the greater the cloud emission. Figure 3 shows the ratio of solar reflected radiance to total emitted radiance (surface plus cloud) for two different cloud temperatures and a surface temperature of 290 K. The relative contribution of emission and reflection to the total signal is seen to be about equal for the warmer cloud when the effective radius is 10 μm (Fig. 3b). For the colder cloud at 275 K (Fig. 3a), the reflected component dominates when effective radii are

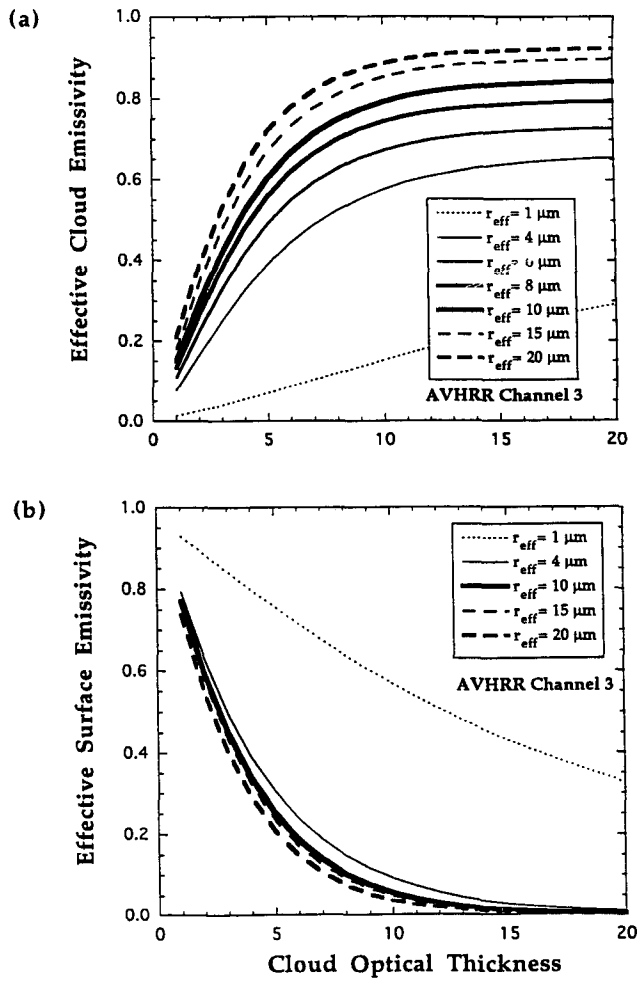

FIG. 2. AVHRR channel 3 effective emissivities for (a) cloud and for (b) surface for various effective radii r_{eff} as a function of cloud optical thickness for the same conditions as Fig. 1.

smaller than 15 μm. A similar calculation at the same two cloud temperatures is made for a surface temperature of 270 K and is shown in Fig. 4. For a thick cloud, all ratios in Figs. 3a and 4a are equivalent since the same cloud temperature is used in both instances and the contribution from the surface is zero—likewise for Figs. 3b and 4b. At moderate thicknesses, there is a trade-off between less surface emission and greater cloud emission; depending on actual temperatures, net emission can increase or decrease rapidly with optical thickness. For the examples shown, the reflectance-to-emission ratio reaches its asymptotic limit quicker for the colder surface, as total emission decreases more quickly with optical thickness, than for the warmer surface. A peaking in the ratio is seen for the colder surface at an optical thickness of about 3–5.

It is clear that emission in the 3.7-μm channel is significant and must be removed to resolve the reflected signal and infer droplet size. Without direct tempera-

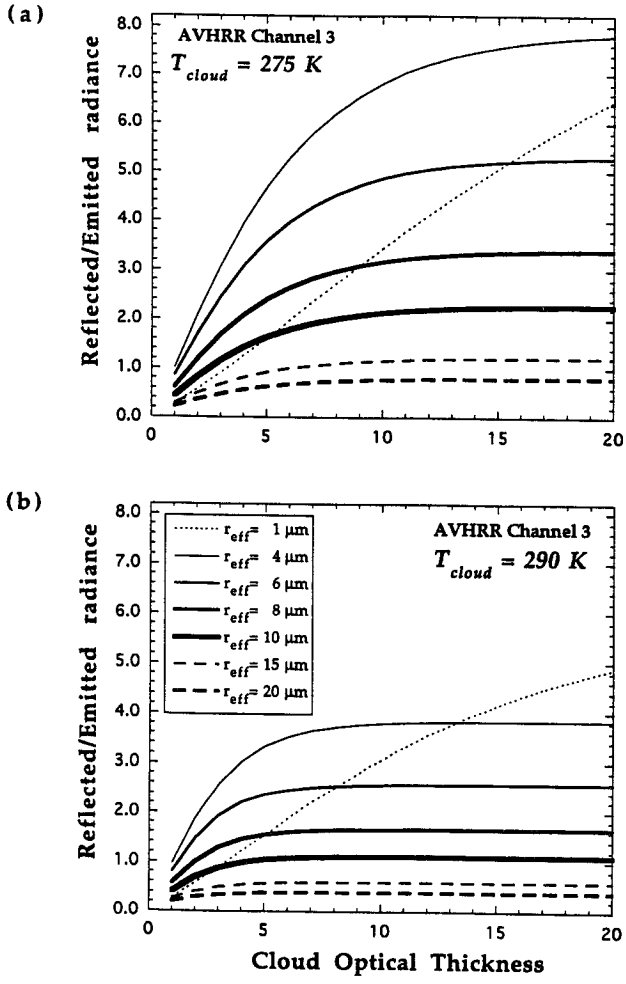

FIG. 3. The ratio of reflected to emitted radiance for AVHRR channel 3 for various effective radii r_{eff} as a function of cloud optical thickness, for a surface temperature of 290 K and cloud temperatures of (a) 275 K and (b) 290 K. Other conditions are the same as in Fig. 1.

ture measurements, the remote sensing algorithm must include a thermal channel for inferring cloud and surface temperatures; AVHRR channel 4 ($\approx$11 μm) can be used for this purpose. Effective emissivities have been calculated for this channel in a manner identical to the 3.7-μm channel. As an example, the radiative temperature is plotted in Fig. 5 for a surface temperature of 290 K and a cloud temperature of 280 K. Once again, the presence of a thin cloud complicates the analysis. In this case, cloud-top temperature will be overestimated for small optical thicknesses by an amount depending on droplet size. For example, a cloud with an effective radius of 6 μm and an optical thickness of 4 will present a radiative temperature about 2° higher than the actual cloud temperature. For the present study, cloud-top temperatures are specified from the in situ aircraft measurements.

The finite bandwidth of the AVHRR channels was taken into account for all reflectance and emission calculations. The details are given in the next section.

3. The remote sensing algorithm

The creation of a library of reflectances and emissivities at a number of effective radii, optical thicknesses, and solar and satellite viewing geometries constitutes the *forward* part of the algorithm and is calculated using the doubling or adding matrix method of Twomey et al. (1966). In this study, the *inverse* problem is solved by finding the best match between the measured satellite quantity for the pixel being analyzed in the AVHRR image and an entry in the library. The radius and optical thickness corresponding to this entry becomes the solution. For clouds that are not optically thick, the effect of the surface on cloud-top radiances complicates the interpretation of the signal in all channels. This is especially true for emission in the 3.7-μm and thermal IR channels where surface emission is

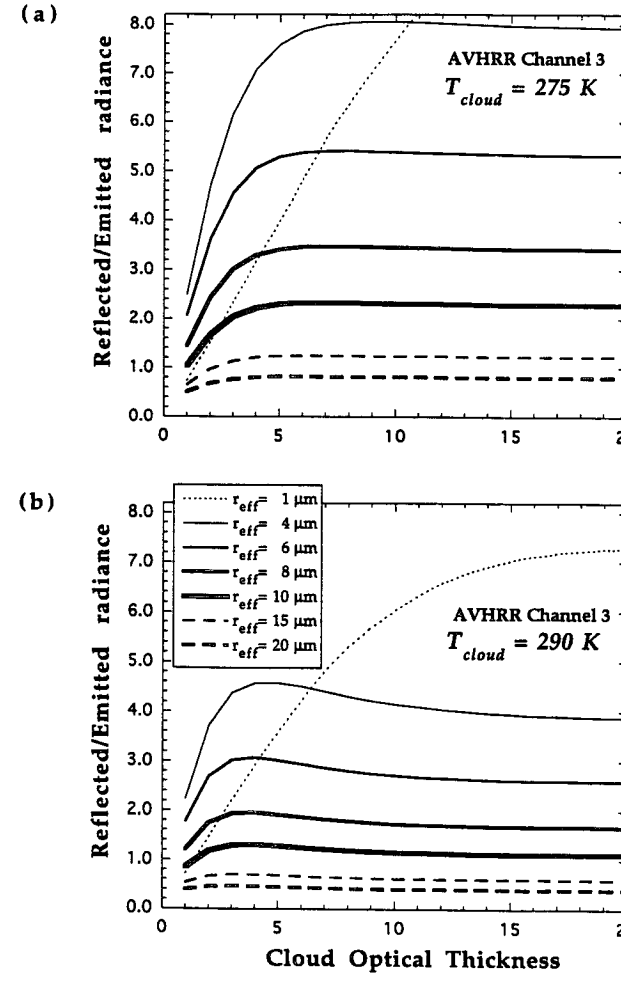

FIG. 4. Same as Fig. 3 but for a surface temperature of 270 K.

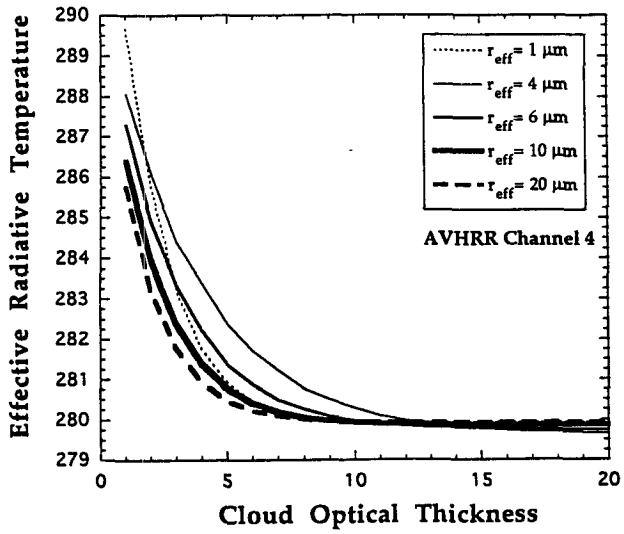

FIG. 5. AVHRR channel 4 effective radiative temperature for various effective radii r_{eff} as a function of cloud optical thickness for a surface temperature of 290 K and a cloud temperature of 280 K. Calculated for a zero surface albedo and $\mu = 0.95$.

likely to be larger than cloud emission. The following general purpose algorithm attempts to account for these difficulties. However, the cloud region analyzed in this study will turn out to have an optical thickness greater than 10 so that the ocean surface will have no effect on the retrieved effective radius and optical thickness (see Figs. 1–5).

a. *The forward problem*

The processes involved in the calculation of reflectance and emissivity libraries are shown schematically in Fig. 6. The starting point for all calculations is the complex refractive index of water. The compilation of Irvine and Pollack (1968) is used; in the 3.7-μm band, the absorption measurements of Downing and Williams (1975) agree well with those given by Irvine and Pollack. In addition to the optical constants, the droplet size distribution is needed for determining the Mie parameters ϖ_0, Q_e, and the phase function. Two moments of the size distribution, the effective radius and effective variance v_{eff}, are specified using a Gamma distribution (Hansen and Travis 1974). A fixed effective variance of 0.05 and effective radii in 1-μm increments are used in calculating the Mie parameters at various wavelengths in each channel. These parameters are then input to a radiative transfer code (Twomey et al. 1966) along with specified geometries and a fixed surface albedo. The cosine of the solar and satellite viewing angles, μ_0 and μ, respectively, are limited to $\mu_0 = 0.25, 0.35, \cdots, 0.95$ and $\mu = 0.55, 0.65, \cdots, 0.95$. An interpolation on these angles is used when analyzing data. The dependence of reflectance on the azimuthal angle ϕ is found using a Fourier series containing harmonic bidirectional reflectances. For an ocean surface, a fixed Lambertian surface albedo of 0.06, 0.01, and 0.0 was used for AVHRR channels 1, 3, and 4, respectively. Clear-sky AVHRR ocean radiances viewed in the antisolar direction were consistent with these albedos when using a nominal atmospheric correction to be described later. Reflectance or emissivity is then calculated at a given wavelength for optical thicknesses 1, 2, ... up to the asymptotic limit (or to a thickness where larger increments are satisfactory) and all combinations of r_{eff}, μ_0, and μ.

The spectral response of each channel (Kidwell 1991) can be important, especially in the 3.7-μm channel where water absorption changes substantially over the approximately 300-nm bandwidth of the channel. A simple integration using calculations at five equally spaced wavelengths within the channel is used. For example, spectrally averaged reflectance includes a solar flux weighting and is approximated as

$$\frac{\sum_{k=1}^{5} F_{0_{\lambda_k}} \Phi_{\lambda_k} R_{\lambda_k}}{\sum_{k=1}^{5} F_{0_{\lambda_k}} \Phi_{\lambda_k}}, \qquad (2)$$

where the incoming solar flux is F_0 and Φ is the channel's spectral response. It is this calculation of reflectance that is stored in the library for channels 1 and 3. Note that the equation is not the spectrally averaged reflectance, which the satellite cannot measure, but is

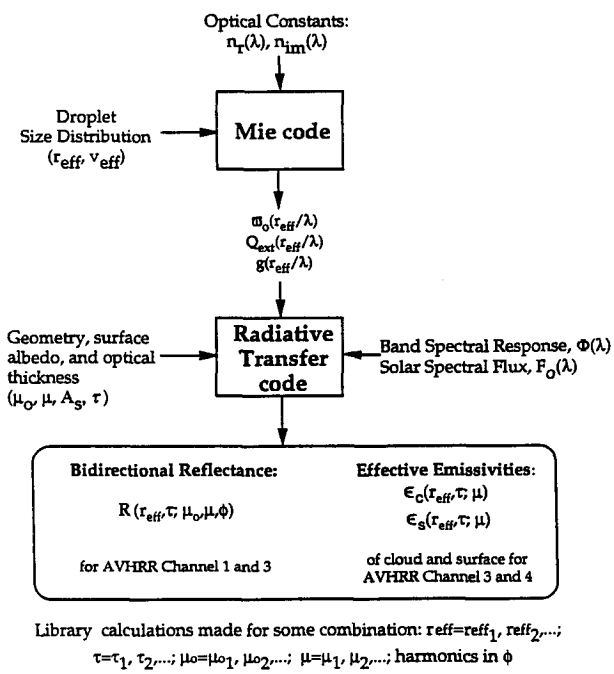

FIG. 6. A schematic representation of the algorithm used for calculating the reflectance and emissivity libraries.

proportional to the net reflected radiance in the channel, which the satellite *does* measure, divided by the net solar input flux in the channel. The total radiance in the 3.7-μm channel 3 is usually expressed as a radiative temperature, by virtue of its onboard blackbody calibration, but can be converted to the average radiance in the band (Planet 1988). The band-averaged channel 3 radiance is the product of $\mu_0\langle F_0\rangle_\lambda/\pi$ with Eq. (2), where $\langle F_0\rangle_\lambda$ represents the channel 3 band-averaged incoming solar flux, $\Sigma_k F_{0\lambda_k}\Phi_{\lambda_k}/\Sigma_k \Phi_{\lambda_k}$ ($F_{0\lambda}$ taken from Thekaekara 1969). With reflection, the incident solar spectral flux is known and the integration (summation) over wavelength can be calculated before any data are processed. For the effective emissivities, the relative spectral response of the Planck function across the channel is unknown until the cloud and surface temperatures of the scene are determined. The temperature is unknown a priori, so emission cannot be taken out of the summation. However, for channels 4 and 5 ($\approx$12 μm), the Planck function across the band varies by less that 3% from the midband value for a temperature of 300 K, and by less than 0.5% at 273 K. But the Planck function has a strong wavelength dependence across the channel 3 band, varying by as much as 50% from midband values. Fortunately, the ratio of Planck radiance at any in-band wavelength to the midband Plank radiance is well within 10% for all temperatures from 273 to 300 K, so the emitted radiance in channel 3 can be approximated as

$$B_{\lambda_3}\left[\frac{\sum_{k=1}^{5}(B_{\lambda_k}/B_{\lambda_3})\Phi_{\lambda_k}\epsilon_{\lambda_k}}{\sum_{k=1}^{5}\Phi_{\lambda_k}}\right], \qquad (3)$$

where B is the Planck radiance, ϵ is effective emissivity discussed in the last section, and λ_3 is the midband wavelength. The ratio of Planck radiances for the different wavelengths needs only be calculated once at an appropriate temperature—for example, 283 K. With this formulation, absolute emission is removed from the summation and the term in brackets, representing a band-averaged effective emissivity, and is stored in the library for both the cloud and surface.

b. *The inverse problem*

The determination of optical thickness and effective radius from the best fit between the satellite data and library entries is shown schematically in Fig. 7. The notation R_i^{calc}, $\epsilon_{c_i}^{\text{calc}}$, and $\epsilon_{s_i}^{\text{calc}}$ represents the *calculated* bidirectional reflectance, effective cloud emissivity, and effective surface emissivity, respectively, for AVHRR channel i; the same notation with superscript "meas" represents the *measured* quantities. Calculations are valid for a cloud with no intervening atmosphere, and so actual satellite measurements must be extrapolated to cloud top. The influence of the atmosphere below cloud, which can be combined with the surface albedo if necessary, is ignored. The solution is determined from the minimum residual defined in Fig. 7 and applied to each entry in the library. The weights for channels 1 and 3, W_1 and W_3, respectively, were chosen such that each channel has roughly equivalent influence. The solutions were not sensitive to the exact choice of weightings or residual definition (relative reflectance differences were also used). With these weightings, contours of constant residual in τ and r_{eff} space show a well-defined minimum. However, a secondary minimum is often found at a small *incorrect* radius,—for example, 1 μm—and a small optical thickness. This problem was mentioned in section 2 and is obvious from inspection of Fig. 1b. The spurious solution is not limited to 3.7-μm retrievals [see Twomey and Cocks (1989); Nakajima and King 1990]. For marine stratocumulus clouds, the minimum residual for a 1-μm size can be disregarded. Note from the schematic that in each calculation of the residual the inferred measurement of the 3.7-μm cloud-top reflectance explicitly depends on the choice of r_{eff} and τ from the library. That is, the partition of measured channel 3 radiance into net emission and cloud reflec-

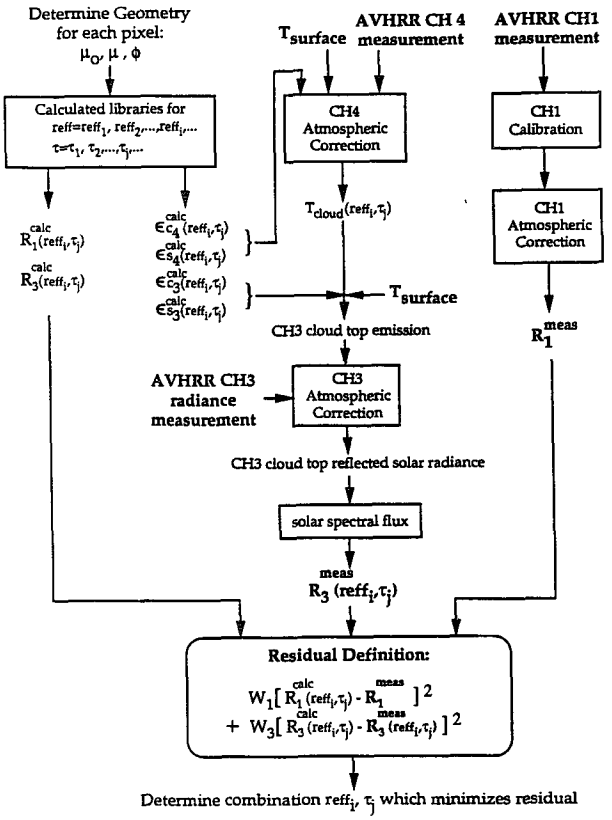

FIG. 7. A schematic representation of the algorithm used for determining effective radius and optical thickness from the measured AVHRR data and the reflectance and emissivity libraries. Measured quantities are shown in boldface.

tance depends on the optical thickness and effective radius considered.

Since absolute reflectance is needed for cloud retrievals, the measured cloud-top reflectance in channel 1, shown to the far right of the figure, is influenced by the channel's calibration. Unfortunately, the AVHRR lacks onboard calibration. Absolute reflectance is usually estimated through in-flight calibrations made with scenes of known reflectance such as White Sands, New Mexico, (Teillet et al. 1990; Che and Price 1992; Abel et al. 1993) or ocean surfaces (Kaufman and Holben 1993). These studies have all shown a significant decrease in sensor gain compared with preflight calibrations. No calibration has been reported for the *NOAA-12* AVHRR used in this study. We make use of our own calibrated, nadir-pointing, visible radiometer, with spectral characteristics similar to channel 1, that flew onboard the NASA ER-2. An in-flight calibration has been made with the radiometer using clouds as the common reflectance target. The calibration uses the same cloud chosen for retrieval validation and so has the advantage of being made simultaneously with the other measurements. The results of this in-flight calibration are presented in section 5.

As noted in Fig. 7, atmospheric corrections are important to all channels. A rigorous correction would need the angular scattering and transmission functions for some specified atmosphere *added* to the complete bidirectional reflectance matrix for the cloud. Such a calculation would best be made at the library level; that is, a complete library would have to be calculated each time a new atmosphere is encountered. Since the exact state of the atmosphere, such as aerosol and water vapor loading, is not usually known anyway, such a detailed correction does not seem warranted. A simplified approach has been adopted that allows the library to be decoupled from the atmosphere. For example, in the visible channel, the satellite sees a bidirectional reflectance approximated by

$$R(\mu_0, \mu, \phi) = R^{\text{cloud}}(\mu_0, \mu, \phi)t(\mu_0)t(\mu) + R^{\text{atm}}(\mu_0, \mu, \phi), \quad (4)$$

where R^{cloud} is the cloud reflectance, in the absence of an atmosphere, that is stored in the library and R^{atm} accounts for scattering directly from the atmosphere. One-way atmospheric transmission t in the channel is shown as a scalar and does not account for the full angular distribution of energy or multiple reflections between the atmosphere and the cloud. However, the transmission term $t(\mu_0)$ can include diffuse as well as direct transmitted flux to help account for energy scattered by the atmosphere onto the cloud. Similar atmospheric approximations have been used by Kaufman and Sendra (1988), Saunders (1990), Fraser et al. (1992), and Mitchell and O'Brien (1993). In the 3.7-μm channel, where both emission and solar reflectance are important, the satellite radiance is approximated as

$$I(\mu_0, \mu, \phi) = I^{\text{cloud}}_{\text{scat}}(\mu_0, \mu, \phi)t(\mu_0)t(\mu) + I^{\text{atm}}_{\text{scat}}(\mu_0, \mu, \phi) + I^{\text{atm}}_{\text{emit}}(\mu) + I^{\text{cloud}}_{\text{emit}}(\mu)t(\mu), \quad (5)$$

where both the cloud and atmosphere contribute emitted (I_{emit}) and solar scattered (I_{scat}) energy. In the thermal IR only the emission terms in Eq. (5) are needed. The atmospheric terms in Eqs. (4) and (5) were modeled using the LOWTRAN 7 radiation code (Kneizys et al. 1988). The atmospheric path was taken to be from cloud top to the top of the atmosphere. Both midlatitude summer and winter standard atmospheres were analyzed, along with low-level temperature and moisture soundings taken from Santa Maria at noontime on the day of the validation (Syrett 1993). Nominal atmospheric corrections used in this study, based on the midlatitude summer and low-level sounding analysis, are shown in Table 1 (for $\mu \approx 1$ and $\mu_0 \approx 0.6$). The visible atmospheric reflectance is consistent with clear-sky reflectances seen over the ocean and the model calculations of Fraser et al. (1992). Solar transmittance in channel 1 includes an approximation for the diffuse transmission, about 10% of the direct transmittance at cloud top, found from a full multiple-scattering code. This gives an effective transmittance in channel 1 that is equivalent for both the $\mu \approx 1$ and $\mu_0 \approx 0.6$ paths. In channel 3, the mean transmittance for the two angles is shown. The direct transmittances compare relatively well with the AVHRR line-by-line calculations of Saunders and Edwards (1989). The uncertainties assigned to these values, based on calculations from the different atmospheric profiles, and their effect on cloud retrievals will be addressed in section 4.

4. Uncertainty analysis

a. Uncertainty in the retrieval of optical thickness

Visible channel reflectance uncertainties primarily affect the accuracy in retrieving optical thickness. As can be seen from Fig. 1a, large changes in optical thickness can occur for small changes in reflectance for thick

TABLE 1. Nominal atmospheric quantities used in approximating cloud-top properties from satellite measurements, along with assumed uncertainties used in the error analysis of section 4.

AVHRR channel	Quantity	Nominal value	Assumed uncertainty (±%)
1	Transmittance	0.88	5
3		0.82	5
4		0.88	5
1	Atmospheric reflection	0.025	50
3		0.001*	50
3	Atmospheric emission	0.030*	50
4		10.5*	50

* In units of m W-m^{-2}-sr-cm^{-1}.

clouds, while optical thickness has little sensitivity to reflectance for thin clouds. Uncertainty in the surface albedo (see Fig. 6) dominates for the thinnest clouds. Figure 8a shows the effect on retrieved optical thickness of a ± 0.04 error in the assumed albedo of 0.06 used for the ocean surface. For $\tau > 5$, errors are less than 10% but can increase to 100% for $\tau = 1$. This error depends very little on effective radius as expected from Fig. 1a. The analysis assumes that the effective radius is known and that the surface is still Lambertian. While this uncertainty in surface albedo is a *model* error, the channel's calibration and the atmospheric correction (see Fig. 7) act together as direct sources of *measurement* error for cloud-top reflectance. Figure 8b shows optical thickness retrieval errors for $\pm 5\%$ and $\pm 10\%$ errors in the measured channel 1 cloud reflectance. Absolute error increases rapidly with optical thickness. Again, there is little dependence on radius. In these examples, for $\tau \approx 5$, a reflectance measurement error of 10% will cause as much uncertainty in retrieved optical thickness as an error of 67% in the assumed surface albedo. Total retrieval uncertainty can be estimated by combining Figs. 8a,b.

b. *Uncertainty in the retrieval of effective radius*

Uncertainties in the 3.7-μm channel reflectance primarily affect the accuracy in retrieving effective radius. We first look at the model error following Fig. 6 and assume that we have no errors in optical thickness. The first concern is the value for liquid water absorption in the channel. This is difficult to quantify, but since the compilation data of Irvine and Pollack (1968) and the measurements of Downing and Williams (1975) are within a few percent across the channel, this uncertainty is hopefully small. Next, Fig. 6 suggests that uncertainty in effective variance or in the assumption of the size distribution could be a source of error. We estimate these two effects using two different analytic size distributions: Gamma and normal, each with identical effective radii and three effective variances ($v_{\text{eff}} = 0.05$, 0.10, and 0.15). The six distributions are input to the Mie code and used to calculate six libraries. Errors in retrieved effective radius are then evaluated with respect to a retrieval made using a Gamma distribution with an effective variance of 0.10. The size error depends on the effective radius, increasing from near zero for $r_{\text{eff}} = 4$ μm to about 10%–15% for effective radii from 10 to 20 μm for the size distributions and effective variances considered; there is little dependence on optical thickness. As expected, the error is primarily dependent on effective variance and not the details of size distribution (Hansen and Travis 1974). However, there can be appreciable error for different distributions with the same effective variance. For example, it was found that a normal distribution with $v_{\text{eff}} = 0.10$ would cause a retrieved radius to be between 0.2 and 0.5 μm too large when using the reference distribution (Gamma distribution with $v_{\text{eff}} = 0.10$). As another example, a size distribution with $r_{\text{eff}} = 10$ μm was found in the measured FSSP data taken by the University of Washington C-131A in the cloud region discussed in the next section. This actual size distribution would cause the retrieved radius to be 0.5 μm too large when the retrieval is made with the incorrect reference library.

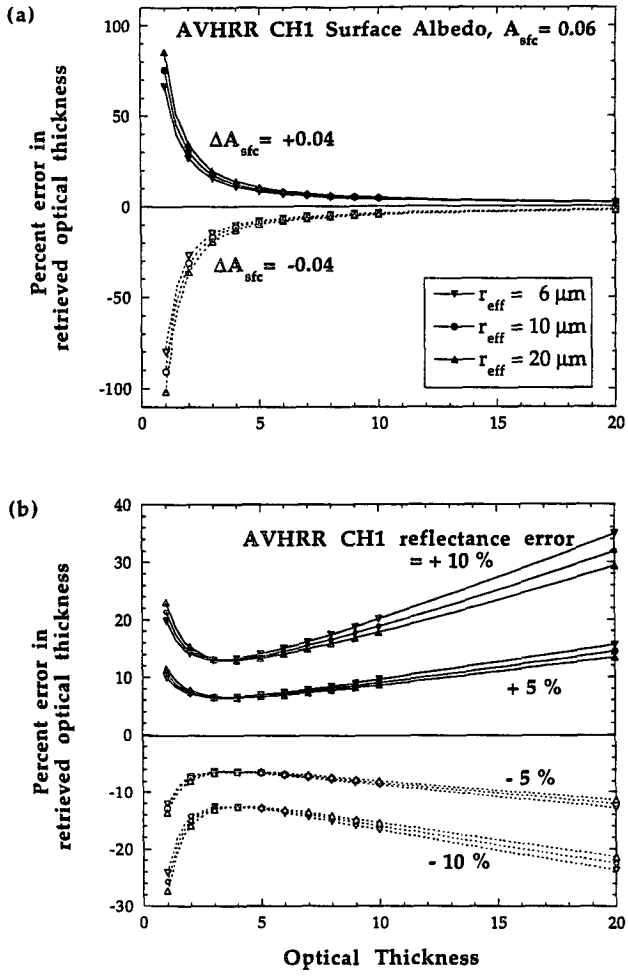

FIG. 8. Error in retrieval of cloud optical thickness for various effective radii r_{eff} as a function of optical thickness for (a) an uncertainty in surface albedo of 0.06 $\pm$ 0.04, and (b) a $\pm 5\%$ and $\pm 10\%$ error in measured AVHRR channel 1 cloud reflectance.

Gaseous absorption inside the cloud will increase the droplet absorption inferred from reflectance measurements and will result in larger retrieved radii. In the 3.7-μm channel, water vapor is the dominant absorber. The cloud is at a relative humidity of 100%, which provides a relatively large absorber amount for a warm cloud. In addition, with multiple scattering and correspondingly longer pathlengths, relatively weak vapor absorption could be elevated to significant levels. Some insight into the problem can be gained by considering the in-cloud path traveled by a reflected photon. For

example, in the 3.7-μm channel the average number of scatterings for a reflected photon is about 8 for an optically thick cloud (compared with 20 for the visible channel at an optical thickness of 10). A photon travels a mean free path of one optical unit inside the cloud, where the optical path is approximately $2\pi r^2 Nl \approx 0.09l$ for the cloud in this study (where l is the geometric path in meters, N is the total droplet concentration of about 100 cm^{-3}, and $r = 11$ μm). The mean free geometric pathlength is then about 13 m, implying an average total path for channel 3 reflected photons of about 100 m. Whether this path is large enough to add significant absorption to reflected photons depends on the absorption coefficient k_v for water vapor at the specified wavelength, pressure, and temperature.

Vapor absorption can be folded into the droplet single-scattering albedo. The average single-scattering albedo over a size distribution is a weighted average of the extinction coefficient (Hansen and Travis 1974). Likewise, for a mixture of constituents—for example, droplets and vapor—the same weighting can be used (Tsay et al. 1989). With k_e as the extinction coefficient, the effective single-scattering albedo ϖ_0^* for the mixture becomes

$$\varpi_0^* = \frac{\sum_i \varpi_{0_i} k_{e_i}}{\sum_i k_{e_i}}. \tag{6}$$

Let k_v and k_d be the extinction coefficients for vapor and droplets, respectively. With the single-scattering albedo for an absorbing vapor molecule being zero, Eq. (6) reduces to

$$\varpi_0^*(k_v) = \frac{\varpi_0}{1 + \dfrac{k_v}{k_d}} = \frac{\varpi_0}{1 + \dfrac{k_v}{Q_e \pi r^2 N}} = \frac{\varpi_0}{1 + \dfrac{4\rho_l r}{3WQ_e} k_v}, \tag{7}$$

where ϖ_0 is for the droplets only, and the last form is expressed in terms of liquid water content W and the density of liquid water ρ_l. Note that the first form can also be expressed in terms of mean free paths as $\varpi_0/(1 + \bar{l}_d/\bar{l}_v)$. Then, for a constant liquid water content, the droplet mean free geometric path increases with effective radius and the effective single scattering albedo decreases. Equation (7) is valid for a single wavelength. The net effect of vapor absorption averaged over the 3.7-μm channel is analyzed using a k-distribution method (Arking and Grossman 1972). The statistics of the absorption coefficient across the band are binned to form a probability distribution $p(k_v)$ for the likelihood of a particular k_v value being found. Integration over wavelength is then expressed as an integration over k_v, and Eq. (7) becomes

$$\varpi_0^* = \int \varpi_0^*(k_v) p(k_v) dk_v, \tag{8}$$

where ϖ_0^* is understood to depend on effective radius. A k probability distribution found from line-by-line code for vapor at a temperature of 285 K, a pressure of 950 mb, and a relative humidity of 100% is shown in Fig. 9a. Equation (8) was then calculated for a range of radii and $W = 0.3$ g m^{-3}. The resulting bias in retrieved radius is shown in Fig. 9b for a thick cloud. The bias can be approximated for an optically thick cloud as $\Delta r_{\text{eff}} \approx (\varpi_0 - \varpi_0^*)/gk_l$, where g is the droplet's asymmetry parameter and k_l is the bulk absorption coefficient for water (derived from approximations given by Twomey and Bohren 1980). Since droplet absorption is proportional to effective radius, the bias is approximately linear with droplet size as Fig. 9b demonstrates. Absolute bias error is less than 0.3 μm for $r_{\text{eff}} < 15$ μm, and relative error is less than 3% for 4 μm $< r_{\text{eff}} <$ 25 μm. Adding continuum absorption, as parameterized in LOWTRAN for the 3.7-μm band, increases the bias by less than 0.1 μm for all effective

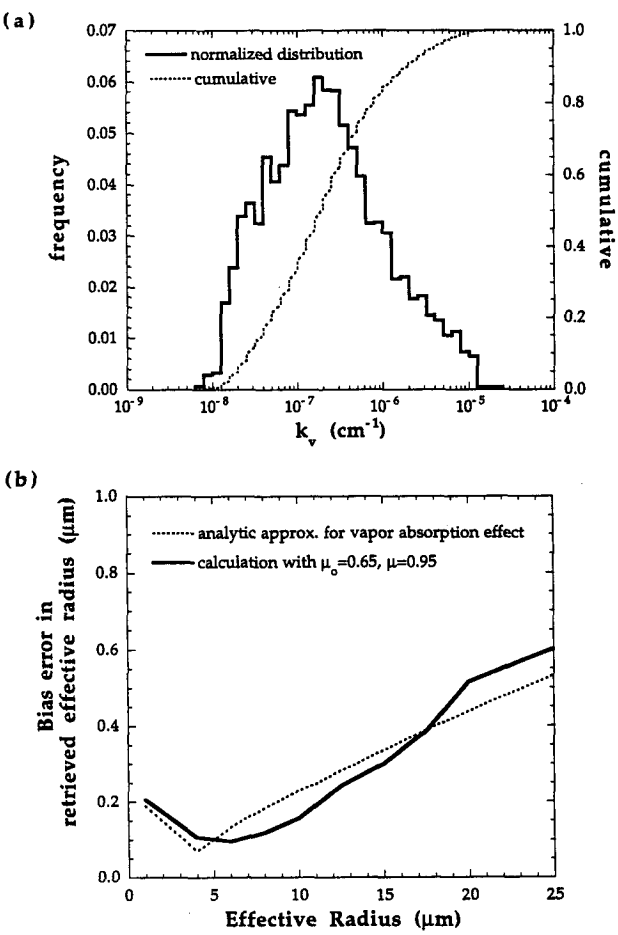

FIG. 9. (a) AVHRR channel 3 k probability distribution for a pressure of 950 mb, temperature of 285 K, and relative humidity of 100%. Determined from line-by-line data at 5000 wavenumbers across the channel. (b) Resulting droplet size bias error due to in-cloud vapor absorption.

radii. So in-cloud vapor absorption does not appear to be a significant source of size retrieval error.

The calculation of reflectance involves a spectral averaging across the channel. For channel 3, liquid water absorption increases quickly when moving away from the channel center, so a reflectance calculation made only at band center would underestimate channel absorption, overestimate reflectance, and therefore infer larger droplet sizes. The retrieval error using a single wavelength calculation for reflectance versus an integration over the channel (approximated with an 11-wavelength calculation) was determined as a function of effective radius. For an optically thick cloud, if a 10-μm radius is retrieved using a reflectance library calculated only at 3.75 μm, the retrieval using the *NOAA-12* AVHRR channel 3 band-averaged reflectance would be about 1 μm smaller, or 9 μm. A similar overestimation of about 10% was found for effective radii from 5 to 20 μm. These errors have little dependence on solar zenith angle and tend to decrease somewhat for optically thin clouds. In addition, channel 3 emission is very sensitive to wavelength, being on the steep slope of the Planck curve, and spectral averaging of the effective emissivities is particularly important. It was determined that some type of spectral averaging is necessary and the 5 wavelength averages of Eqs. (2) and (3) were deemed sufficient.

Errors in the laboratory measurement of the channel 3 bandpass, or an in-flight spectral shift, are also a concern. As an example, the bandpass of channel 3 for *NOAA-12* is shifted upward about 40 nm compared with *NOAA-11* (Kidwell 1991), resulting in significant differences in both cloud reflectance and emission. Band-averaged *NOAA-12* channel 3 reflectance and emission are larger than *NOAA-11* calculations by about 9% and 14%, respectively, for expected droplet sizes (calculated for a range of optical thicknesses and angles). The reflectance difference alone would account for retrieved droplet size differences of about 5% between the two instruments. However, including the larger emission for the *NOAA-12* channel greatly increases the retrieval difference. If, for example, a cloud retrieval using *NOAA-12* reflectance and emissivity libraries inferred an effective radius of 11 μm, as occurs in the validation of the next section, a retrieval with a *NOAA-11* library would infer a size of only about 10 μm. If *NOAA-12* libraries retrieve 13 μm, a *NOAA-11* library would infer 11 μm. These differences are valid for the 10°C cloud studied in the validation; warmer or colder clouds would increase or decrease this size difference, respectively. Obviously, accurate knowledge of the in-flight channel 3 bandpass is important.

Error in the channel 3 atmospheric corrections, diagramed in the schematic of Fig. 7, act as a direct source of uncertainty in inferring cloud-top radiance (see Fig. 1b). The accuracy of the onboard blackbody calibration and errors in the inference of cloud-top temperature by channel 4, needed for eliminating channel 3 cloud emission, are also a concern. Together, all three combine to create an uncertainty in the 3.7-μm cloud-reflected radiance. Figure 10 shows calculations of effective radius retrieval errors for $\pm 5\%$, $\pm 10\%$, and $\pm 15\%$ errors in the channel 3 cloud reflectance, as a function of the actual effective radius, for an optically thick cloud. Relative error is nearly constant for $r_{\text{eff}} > 8$ μm, ranging from about 4% to 14%. For smaller radii, relative errors increase to 10%–30%.

The analysis of this section gives some quantitative feel for the various contributions to error. As an example, consider all discussed sources of effective radius retrieval error, both modeled and measured, for an optically thick cloud (i.e., $\tau > 6$) with $r_{\text{eff}} = 10$ μm to 13 μm. Expected uncertainties based on results given in this section are the following: for $\pm 15\%$ channel 3 cloud reflectance error $\sim \pm 13\%$ retrieval error in droplet size; in-cloud vapor absorption $\sim +3\%$ error; size distribution uncertainties $\pm 10\%$ error. In absence of other measurements, the worst case net uncertainty for this example ranges from -20% to $+25\%$ (or absolute uncertainty from about -2.3 μm to $+3.0$ μm). For the validation of the next section, channel 3 reflection uncertainties have been reduced substantially with in situ cloud temperature measurements. Also, cloud effective variance has been calculated from FSSP measurements, hopefully reducing this source of uncertainty.

The largest errors for both optical thickness and effective radius come from the uncertainty in cloud-top reflectance that in turn comes from uncertainties in atmospheric corrections and calibrations. Another way to quantify this component of retrieval uncertainty is by repeatedly applying the retrieval algorithm to the same

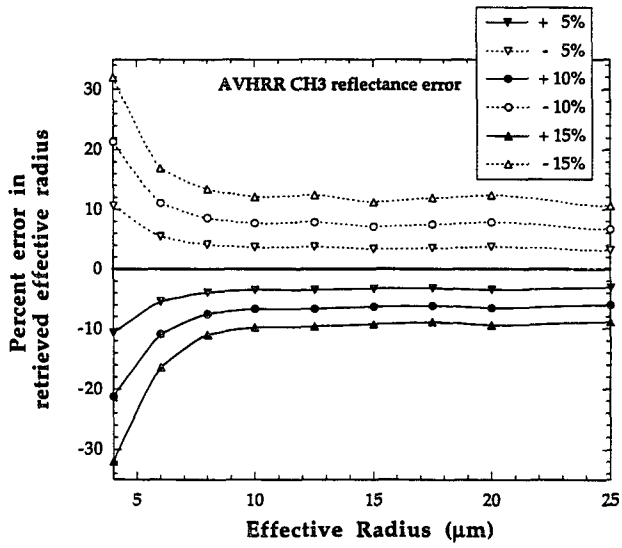

FIG. 10. Error in retrieval of cloud effective radius as a function of effective radius for an uncertainty in AVHRR channel 3 cloud reflectance of $\pm 5\%$, $\pm 10\%$, and $\pm 15\%$. Calculated for an optically thick cloud for channel 3 ($\approx \tau > 6$).

satellite measurement while randomly varying atmospheric corrections and channel calibration according to some assumed statistics. First, the satellite signals seen for a cloud with $r_{eff} = 11$ μm and $\tau = 15$ (parameters retrieved in the next section) are determined using the nominal atmospheric corrections of Table 1. The uncertainty assumed for each entry is also given in this table, and an uncertainty of $\pm 6\%$ is used for the AVHRR channel 1 calibration (discussed in the next section). During each run of the algorithm, a value for each quantity is randomly chosen from a uniform distribution with limits equal to the assigned uncertainty. First, with application to the validation of the next section, the uncertainty in channel 4 cloud-top temperature is set to zero since in situ temperature measurements are available. Figure 11 shows histograms for optical thickness and effective radius after a few hundred evaluations due to the remaining uncertainties. The histograms are shown for unit bin sizes, though the retrieval library gives results at integer values only. The standard deviations for optical thickness and effective radius are 2.1 and 0.7 μm, respectively, with maximum deviations from the average being -4 to $+7$ in thickness and -1 to $+2$ μm in size (about the same as the predictions made above). Both histograms are skewed to larger values, showing the increase in absolute error that occurs for larger droplets or thicknesses as seen in Figs. 8b and 10. These results serve as error bars for the validation of the next section but of course are meaningful only if the nominal corrections and uncertainties are appropriate for the season and location of the retrieval. It is important to realize that if cloud-top temperature was not available and the channel 4 atmospheric corrections and uncertainties of Table 1 were used, then the standard deviation in the size retrieval increases threefold to about 2 μm, with maximum deviations from the 11-μm average being -2 to $+7$ μm. In this case, the sensitivity of the size retrieval to atmospheric corrections would be dominated by the channel 4 inference of cloud-top temperature.

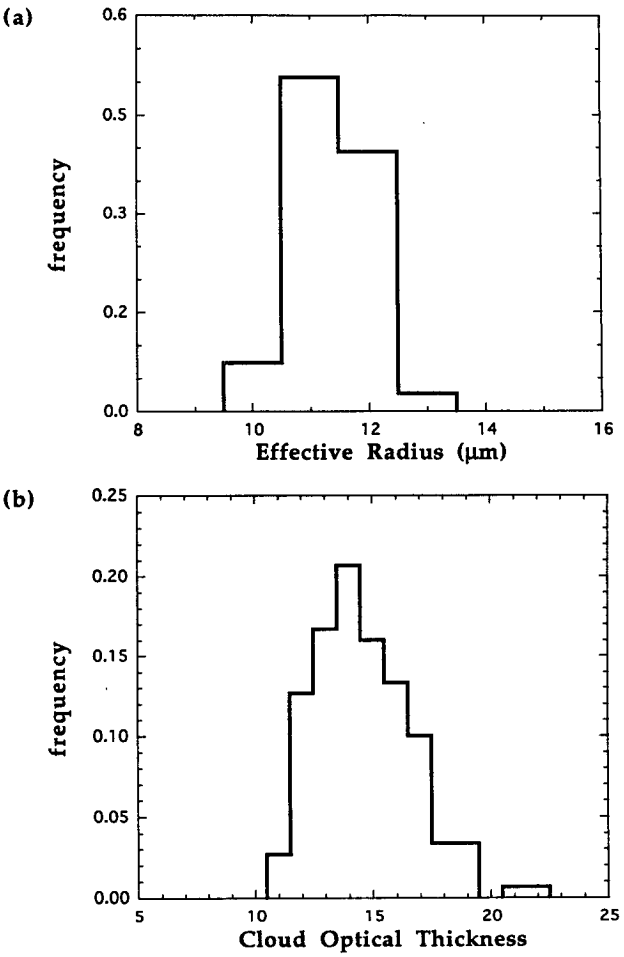

FIG. 11. Histograms for the uncertainty in the retrieved (a) effective radius, and (b) optical thickness, using a Monte Carlo statistical analysis with the atmospheric correction uncertainties of Table 1 (excluding AVHRR channel 4 uncertainty) and a channel 1 calibration uncertainty of $\pm 10\%$. The nominal parameters give $r_{eff} = 11$ μm, and $\tau = 15$.

5. Results

On 12 June 1992, a coordinated flight took place with NASA's ER-2, the University of Washington C-131A aircraft, and an overpass of *NOAA-12* at about 0948 UTC over the island of Santa Maria in the Azores (36.9°N, 25.2°W). During this time, the region around Santa Maria was covered with relatively uniform boundary layer stratus, while broken cloud dominated the area south of the island. The AVHRR channel 1 image is shown in Fig. 12 where the islands of Santa Maria, Terceira, and Sao Miguel are indicated. A surface high pressure was located near 33°N, 30°W, and low-level winds at Santa Maria were out of the north-northeast. Surface back trajectories indicated that the air over the last few days had come out of the west-northwest (Bluth and Albrecht 1993). A cloud lidar system (Spinhirne et al. 1989) aboard the ER-2 detected no cirrus or other higher-level cloud during its flight. The lidar placed the stratocumulus cloud tops at about 1 km, while the 1200 UTC soundings at Santa Maria showed the cloud-base and cloud-top heights to be at 1 and 1.3 km, respectively (Syrett 1993). The ER-2 took off from the island of Terceira and flew from point A to B in Fig. 12, overflying Santa Maria at the same time as *NOAA-12*. A calibration of the AVHRR channel 1 is made with a visible radiometer flown on the ER-2 using the clouds near point A as the common reflectance target. At the time of the *NOAA-12* overpass, the C-131A aircraft was obtaining cloud microphysical measurements south of Santa Maria toward the edge of the stratus boundary at point C; later in the morning, cloud measurements were made as far east as point D. AVHRR retrievals of cloud optical thickness

FIG. 12. AVHRR channel 1 image of the cloud conditions in the region of Santa Maria Island in the Azores, on 12 June 92 at 0948 UTC. NASA's ER-2 aircraft flew a coordinated flight path from points A to B. The University of Washington C131-A made in situ cloud measurements in a region bounded by Santa Maria, and points C and D.

and effective radius have been made and are compared with the in situ measurements.

a. In-flight calibration of NOAA-12 *AVHRR channel 1*

An absolute calibration of AVHRR channel 1 is necessary for accurate optical thickness retrievals. In-flight calibrations performed on previous instruments indicate that in-flight gain is less than that measured during preflight calibrations (Teillet et al. 1990; Holben et al. 1990; Che and Price 1992; Kaufman and Holben 1993; Abel et al. 1993). For example, channel 1 gain on *NOAA-11* has decreased by about 15% (Abel et al.). There has been no *NOAA-12* in-flight calibration reported in the literature. The stratus cloud deck near point A in Fig. 12 provided a useful target for comparing AVHRR channel 1 reflectances with an ER-2 radiometer.

A visible radiometer with a center wavelength of 590 nm and a bandwidth of 60 nm was developed for use on the ER-2. It was designed with a field of view of 1°, giving a cloud-top resolution of about 300 m compared with the 1.1-km resolution of the AVHRR. The radiometer used a temperature-controlled silicon detector in an evacuated housing sampled at 2 Hz; bandwidth was specified with an interference filter. The radiometer was calibrated with an integrating sphere before and after the experiment, showing a relative change of about 1% between the two calibrations. Clouds are a particularly good target for in-flight calibrations because reflectance changes little with wavelength throughout the visible and into the near infrared. Therefore, any mismatch between the spectral shape of the two sensors being compared is minimal. In contrast, reflectance targets such as White Sands have significant changes in its spectral reflectance (Abel et al. 1993) in the visible. Cloud bidirectional reflectance was calculated for the ER-2 radiometer bandpass and compared with AVHRR channel 1 calculations (e.g., Fig. 1a). For the optical thicknesses and droplet sizes seen in these clouds, calculated reflectances vary by less than 1% between the two sensors. However, differences in atmospheric transmittance between cloud top and the two sensors, primarily due to stratospheric ozone absorption between the ER-2 flight altitude and the satellite,

have been included to account for spatial and spectral mismatches between the sensors.

The cloud region near point A in Fig. 12 has a relatively uniform reflectance, for both the ER-2 radiometer and the AVHRR, compared with other points along the ER-2 flight path A–B. The ER-2 overflew the site about 4 min before the satellite overpass; both instruments have the same viewing angle at this location ($\mu_{AVHRR} = 0.97$, $\mu_{ER\text{-}2} = 1.0$). Geographic location of satellite pixels is thought to be within 1–2 km using navigational calculations supplied by Durkee (1992, private communication). The ER-2 radiometer shows an average bidirectional reflectance in this location to be 0.496 with a standard deviation of 0.023, based on 300 data points. An AVHRR channel 1 10 × 12 pixel average of this region shows a reflectance of 0.446 with a standard deviation of 0.021; the AVHRR reflectances have little dependence on the exact pixels chosen for the average. When including nominal atmospheric corrections to both sensors, the reflectance seen by the ER-2 radiometer is about 13% larger than that measured by the AVHRR using prelaunch calibration constants. Alternatively, channel 1 gain has been reduced by about 11% when referenced to the ER-2 radiometer. A definitive uncertainty for this calibration is difficult since it requires knowing the uncertainties associated with each quantity affecting the calibration. One estimate of uncertainty was made with a Monte Carlo statistical analysis using uniform probability distributions for the following assumed uncertainties: a ±5% uncertainty assigned to the calibration of the ER-2 radiometer (includes the sphere's absolute calibration at ±2%, and error in transferring the sphere calibration to the radiometer); uncertainties in sensor measurements of cloud reflectance were set to the observed standard deviations; atmospheric transmittance uncertainty was set to ±5%. Then the in-flight calibration would have an expected standard deviation of 5.5%.

b. In situ microphysical measurements

A new microphysical probe, Gerber Scientific's Particulate Volume Monitor (PVM-100A), was flown on the C-131A during ASTEX. The probe measured integrated droplet surface area and cloud liquid water content at a 10-Hz sampling rate and a relatively large sampling volume of about 1.25 cm^3 (Gerber et al. 1994). Effective radius is calculated from a ratio of liquid water content to surface area. Gerber et al. reported that the PVM-measured effective radius was about 40% higher than measurements made with the FSSP-100. Figure 13 shows the vertical profile of effective radius soon after takeoff as measured by both instruments. The cloud is about 300 m thick in agreement with the sounding data from 1200 UTC. Effective radius almost doubles in going from cloud base to cloud top. At the same time, liquid water content increased with height from 0.1 to 0.5 g cm^{-3}, while total droplet

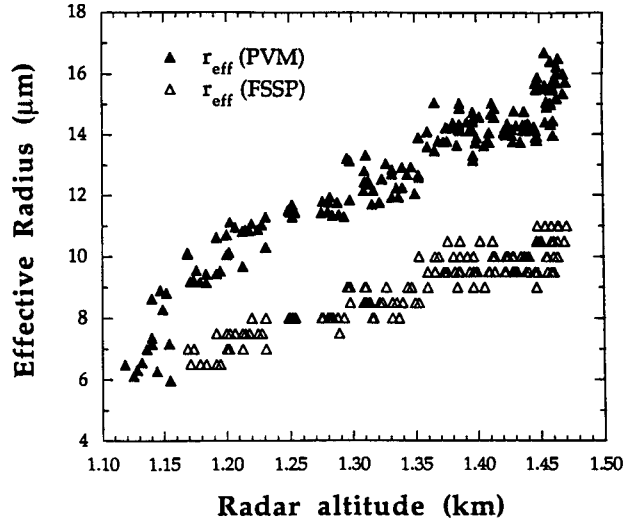

FIG. 13. Effective radius as a function of vertical position in the cloud, as measured by the PVM and FSSP instruments, near Santa Maria at 0940 UTC.

number concentration, derived from the FSSP, remained constant at about 150 cm^{-3}. Using the profile of PVM-measured liquid water content and effective radius, optical thickness is calculated to be about 13. With FSSP-measured effective radius and liquid water content, calculated optical thickness increases to about 17. It is clear that the altitude of the aircraft in the cloud must be considered when using the data. Based on the asymptotic thicknesses seen for the 3.7-μm reflectance in Fig. 1a, an AVHRR retrieval should give a radius that lies well within an optical depth of 5 from cloud top. This translates to about the upper 100 m of the cloud or an altitude greater than about 1.35 km. A more accurate location for the retrieved radius was found using reflectance calculations that included the vertical structure. The cloud was divided into 10 layers where droplet effective radius and optical thickness were specified using the measured vertical profile. The analysis showed the retrieved radius to be equivalent to the size that is found at an optical depth of 2–3 from cloud top.

At the time of the *NOAA-12* overpass, the C-131A was flying in the stratus about 30 km south of Santa Maria near point C in Fig. 12 (at 36.53°N, 25.18°W) and at an altitude of about 1.4 km. Effective radii, averaged between the times of 0947 and 0953 UTC, were 13.5 μm for the PVM and 9.4 μm for the FSSP, in agreement with the profile of Fig. 13 measured 10 min earlier. Validation of optical thickness is more difficult since an in situ profile must be made. It is assumed that the optical thickness at this location is the same as for the region near Santa Maria where the nearest available profile measurements were taken. The relatively uniform retrieval of optical thickness between the two locations suggest this is a reasonable assumption. The

TABLE 2. Statistics of measured, retrieved, and calculated cloud parameters for the cloud location, designated by point C in Fig. 12, flown in by the C-131A aircraft at the time of the *NOAA-12* overpass (0948 UTC). In situ calculations of optical thickness are based on profile measurements taken 10 min earlier near Santa Maria.

	AVHRR retrieval (3 pixel × 3 pixel average ~ 11 km^2)	Airborne PVM measurements (350 s of data)	Airborne FSSP measurements (350 s of data)
r_{eff} (μm)	11.8	13.5	9.4
σ_{reff} (μm)	0.7	1.5	0.8
τ	14.8	13	17
σ_τ	1.2	—	—

measurements are summarized in Table 2. Between 0953 and 1100 UTC, the C-131A flew south beyond the stratus deck, then back to Santa Maria, east for a distance of over 100 km to point D (at 36.7°N, 23.8°W), and back toward Santa Maria. Measurements taken during this time have been screened for instances when the aircraft was in the upper part of the cloud, between an altitude of 1.35 and 1.50 km, and the PVM-measured liquid water contents were greater than 0.05 g m^{-3}. (A liquid water threshold was used to ensure that the aircraft was flying in the cloud. The exact threshold was not found to affect the statistics.) The statistics for this larger region are given in Table 3, and their histograms are shown in Fig. 14. Average effective radii are very close to those in Table 2, indicating that droplet size statistics appear to be relatively constant across this scale.

c. *AVHRR cloud retrievals*

NOAA-12 AVHRR retrievals of optical thickness and droplet effective radius have been made at the cloud location where in situ microphysical measurements were being taken at the time of the satellite overpass (point C on Fig. 12 at 0948 UTC). Solar and satellite viewing angles are $\mu_0 = 0.63$, $\mu = 0.97$, and $\phi = 10°$. The statistics for a 3 × 3 pixel region, about 11 km^2, were analyzed and are given in Table 2. Though pixel navigation should be within a couple of kilometers, it was comforting to find that there was less than a few percent change in averaged retrievals when expanding to a 7 × 7 pixel area. Retrieved optical thickness is within 14% of the calculations made with either instrument. This discrepancy falls within the expected optical thickness uncertainty shown in Fig. 8b. The figure shows that for a retrieved optical thickness of 15 and a reflectance error of 10%, the optical thickness

TABLE 3. Statistics of measured and retrieved cloud parameters for the large-scale region (bounded by Santa Maria and points C and D in Fig. 12) flown in by the C-131A aircraft between 0940 and 1100 UTC. Statistics for the in situ data are limited to measurements made in the upper part of the cloud, between 1.35 and 1.50 km, when liquid water content exceeded 0.05 g m^{-3}.

	AVHRR retrieval (580 pixels)	Airborne PVM measurements (~1570 s of data)	Airborne FSSP measurements (~1570 s of data)
r_{eff} (μm)	11.0	13.9	9.5
σ_{reff} (μm)	0.7	1.6	2.0
τ	16.2	—	—
σ_τ	3.3	—	—

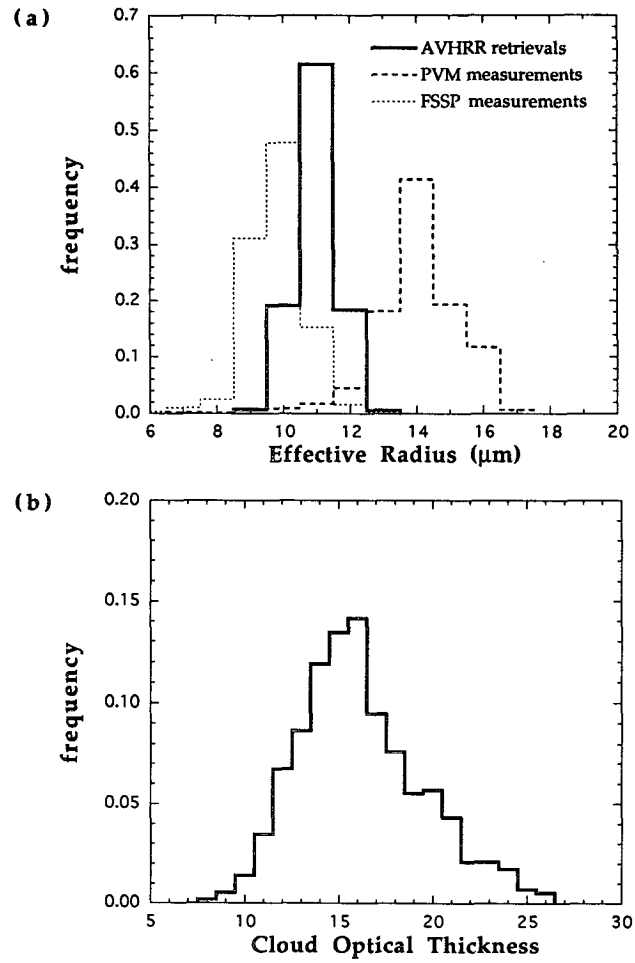

FIG. 14. Histogram of *NOAA-12* AVHRR retrievals of (a) effective radius, and (b) optical thickness, for the cloud region between Santa Maria and points C and D (see Fig. 12). Also shown are PVM and FSSP measurements for selected parts of this region when the University of Washington C-131A was flying in the upper part of the cloud. The statistics are summarized in Table 3.

uncertainty would be about 20%–25%; for a reflectance error of 5%, retrieval uncertainty would be about 10%. Effective radius is about 1.7 μm smaller than the PVM measurements and 2.4 μm larger than the FSSP at this location. Recall from the last section that size retrieval uncertainty was estimated to be about 1–2 μm. The standard deviation for the retrieved effective radius is about the same as seen by both instruments. The effective variance of the droplet size distribution is typically assumed to have little impact on size retrievals and is set to a fixed value. For the cloud location under study, effective variance as calculated with the FSSP averaged about 0.05 and was therefore used in all reflectance library calculations. However, the effective variance was as high as 0.10 at some instances; retrievals using libraries calculated with this larger value increased the retrieved effective radius by about 0.5 μm.

A similar comparison is made in Table 3 for the large-scale cloud region. The upper-cloud in situ measurements show the cloud statistics to be very uniform over the 1.5 h for which the data are analyzed. Because of this observed uniformity, it appears that a reasonably valid comparison can be made between AVHRR retrievals of the large-scale region, applicable only at the time of the satellite overpass, and the in situ data. Because of the temporal differences, it does not seem necessary, or even correct, to analyze only those specific AVHRR pixels that match the flight path of the C-131A. Instead, four AVHRR scan lines in the region, separated by about 10 km, were analyzed for a total of about 580 pixels. The averaged effective radius is now about 0.8 μm smaller than for the specific location reported in Table 2, while averaged optical thickness has increased by 10%. A histogram for both the measurements and retrievals is shown in Fig. 14, indicating that the effective radius retrievals are between the FSSP and PVM measurements.

6. Summary

An algorithm using the AVHRR for retrieving effective radius and optical thickness from solar reflectance measurements has been applied to a relatively homogeneous boundary layer stratus cloud in the vicinity of the Azores on 12 June 1992. AVHRR channel 3 (at 3.7 μm) reflectance provides information primarily regarding droplet size; channel 3 emission is removed using in situ temperature measurements. AVHRR channel 1 (0.65 μm) reflectance contains most of the optical thickness information. An in-flight calibration for channel 1 has been made with a narrowband visible radiometer flown on NASA's ER-2 using the stratus cloud as a reflectance reference. Channel 1 gain was determined to have decreased by about 11% compared with the prelaunch calibration reported by NOAA.

AVHRR retrievals of both effective radius and optical thickness generally lie between the upper-cloud in situ measurements taken by Gerber Scientific's PVM-100A and the Particle Measuring Systems FSSP-100. Compared with the FSSP, PVM-measured effective radius is about 40% larger, while calculated optical thickness is about 25% smaller. Discrepancies between AVHRR retrievals and the upper-cloud in situ measurements are roughly within the expectations of the uncertainty analysis of section 4. Definitive statements concerning the accuracy of the in situ or retrieval measurements are difficult. Both the PVM and the FSSP are, in essence, optical remote sensing instruments and are subject to some of the same theoretical and practical difficulties that crop up in all such techniques. Further, the two instruments have very different sampling volumes, while AVHRR data represent radiances averaged over a 1.1-km footprint with droplet size retrievals weighted to the very upper part of the cloud. The homogeneity of the cloud in this study limited most retrieved effective radii to between 10 and 12 μm, and optical thicknesses between 10 and 20. A more desirable validation would include clouds with a wider range of droplet sizes and thicknesses.

Acknowledgments. We are grateful to Peter Hobbs, A. Rangno, and R. Ferek for providing measurements from the University of Washington C-131A research aircraft and to H. Gerber of Gerber Scientific. We are also indebted to P. Pilewskie, W. Gore, L. Pezzolo, and G. Valero at NASA/ARC for their help with instrument development and calibration, M. King and B. Ridgway at NASA/GSFC for their assistance, and B. Wielicki at NASA/LaRC for helpful comments. The first author would also like to thank the National Research Council research associate program. The research was supported by NASA Contract 460-42-10-10.

REFERENCES

Abel, P., B. Guenther, R. N. Galimore, and J. W. Cooper, 1993: Calibration results for *NOAA-11* AVHRR channels 1 and 2 from congruent path aircraft observations. *J. Atmos. Oceanic. Technol.*, **10,** 493–508.

Arking, A., 1991: The radiative effects of clouds and their impact on climate. *Bull. Amer. Meteor. Soc.*, **71,** 795–813.

——, and K. Grossman, 1972: The influence of line shape and band structure on temperatures in planetary atmospheres. *J. Atmos. Sci.*, **29,** 937–949.

——, and J. D. Childs, 1985: Retrieval of cloud cover parameters from multispectral satellite images. *J. Climate Appl. Meteor.*, **24,** 322–333.

Bluth, R. T., and B. A. Albrecht, 1993: Atlantic stratocumulus transition experiment and marine aerosol and gas exchange June 1992 experiment summary. Part I: Mission summaries. Dept. of Meteorology, The Pennsylvania State University.

Cess, R. D., and Coauthors, 1990: Intercomparison and interpretation of climate feedback processes in 19 atmospheric general circulation models. *J. Geophys. Res.*, **95,** 16 601–16 615.

Che, N., and J. C. Price, 1992: Survey of radiometric calibration results and methods for visible and near infrared channels of *NOAA-7, -9, and -11* AVHRRs. *Remote Sens. Environ.*, **41,** 19–27.

Curran, R. J., and M. C. Wu, 1982: Skylab near-infrared observations of clouds indicating supercooled liquid water droplets. *J. Atmos. Sci.*, **39,** 635–647.

Downing, H. D., and D. Williams, 1975: Optical constants of water in the infrared. *J. Geophys. Res.*, **80,** 1656–1661.

Foot, J. S., 1988: Some observations of the optical properties of clouds. Part I: Stratocumulus. *Quart. J. Roy. Meteor. Soc.*, **114,** 129–144.

Fouquart, Y., J. C. Buriez, M. Herman, and R. S. Kandel, 1990: The influence of clouds on radiation: A climate-modeling perspective. *Rev. Geophys.*, **28,** 145–166.

Fraser, R. S., R. A. Ferrare, Y. J. Kaufman, B. L. Markham, and S. Mattoo, 1992: Algorithm for atmospheric corrections of aircraft and satellite imagery. *Int. J. Remote Sens.*, **13,** 541–557.

Gerber, H., B. G. Arends, and A. S. Ackerman, 1994: New microphysics sensor for aircraft use. *Atmos. Res.*, **30,** 235–252.

Han, Q., W. B. Rossow, and A. A. Lacis, 1994: Near-global survey of effective droplet radii in liquid water clouds using ISCCP data. *J. Climate,* **7,** 465–497.

Hansen, J. E., and J. B. Pollack, 1970: Near-infrared light scattering by terrestrial clouds. *J. Atmos. Sci.*, **27,** 265–281.

——, and L. D. Travis, 1974: Light scattering in planetary atmospheres. *Space Sci. Rev.*, **16,** 527–610.

Holben, B. N., Y. J. Kaufman, and J. D. Kendall, 1990: *NOAA-11* AVHRR visible and near-IR inflight calibration. *Int. J. Remote Sens.*, **11,** 1511–1519.

Irvine, W. M., and J. B. Pollack, 1968: Infrared optical properties of water and ice spheres. *Icarus,* **8,** 324–360.

Kaufman, Y. J., and C. Sendra, 1988: Algorithm for atmospheric corrections of visible and near-IR satellite imagery. *Int. J. Remote Sens.*, **9,** 1357–1381.

——, and B. N. Holben, 1993: Calibration of the AVHRR visible and near-IR bands by atmospheric scattering, ocean glint and desert reflection. *Int. J. Remote Sens.*, **14,** 21–52.

——, and T. Nakajima, 1993: Effect of Amazon smoke on cloud microphysics and albedo—Analysis from satellite imagery. *J. Appl. Meteor.*, **32,** 729–744.

Kidwell, K. B., ed., 1991: *NOAA Polar Orbiter Data Users Guide.* NOAA NESDIS.

King, M. D., Y. J. Kaufman, W. P. Menzel, and D. Tanré, 1992: Remote sensing of cloud, aerosol, and water vapor properties from the Moderate Resolution Imaging Spectrometer (MODIS). *IEEE Trans. Geosci. Remote Sens.*, **30,** 2–27.

Kneizys, F. X., and Coauthors, 1988: Users guide to LOWTRAN 7. AFGL-TR-88-0177, 146 pp.

Knollenberg, R. G., 1981: Techniques for probing cloud microstructure. *Clouds: Their Formation, Optical Properties, and Effects.* P. V. Hobbs and A. Deepak, Eds., Academic Press, 15–91.

Mitchell, R. M., and D. M. O'Brien, 1993: Correction of AVHRR shortwave channels for the effects of atmospheric scattering and absorption. *Remote Sens. Environ.*, **46,** 129–145.

Nakajima, T., and M. D. King, 1990: Determination of the optical thickness and effective particle radius of clouds from reflected solar radiation measurements. Part I: Theory. *J. Atmos. Sci.*, **47,** 1878–1893.

——, ——, J. D. Spinhirne, and L. F. Radke, 1991: Determination of the optical thickness and effective particle radius of clouds from reflected solar radiation measurements. Part II: Marine stratocumulus observations. *J. Atmos. Sci.*, **48,** 728–750.

Planet, W. G., 1988: Data extraction and calibration of TIROS-N/NOAA radiometers. NOAA Tech. Memo. NESS 107-rev. 1, 58 pp. plus appendixes.

Platnick, S., and S. Twomey, 1994: Determining the susceptibility of cloud albedo to changes in droplet concentration with the advanced very high resolution radiometer. *J. Appl. Meteor.*, **33,** 334–347.

Radke, L. F., J. A. Coakley, and M. D. King, 1989: Direct and remote sensing observations of the effects of ships on clouds. *Science,* **246,** 1146–1149.

Rawlins, F., and J. S. Foot, 1990: Remotely sensed measurements of stratocumulus properties during FIRE using the C130 aircraft multi-channel radiometer. *J. Atmos. Sci.*, **47,** 2488–2503.

Saunders, R. W., 1990: The determination of broad band surface albedo from AVHRR visible and near-infrared radiances. *Int. J. Remote Sens.*, **13,** 933–938.

——, and D. P. Edwards, 1989: Atmospheric transmittances for the AVHRR channels. *Appl. Opt.*, **28,** 4154–4160.

Slingo, A., 1989: A GCM parameterization for the shortwave radiative properties of water clouds. *J. Atmos. Sci.*, **46,** 1419–1427.

Spinhirne, J. D., R. Boers, and W. D. Hart, 1989: Cloud top liquid water from lidar observations of marine stratocumulus. *J. Appl. Meteor.*, **28,** 81–90.

Stephens, G. L., and S. Tsay, 1990: On the cloud absorption anomaly. *Quart. J. Roy. Meteor. Soc.*, **116,** 671–704.

Syrett, W. J., 1993: Low-level temperature and moisture structure from ASTEX radiosondes: 1–28 June 1992. Dept. of Meteorology, The Pennsylvania State University.

Taylor, J. P., 1992: Sensitivity of remotely sensed effective radius of cloud droplets to changes in LOWTRAN version. *J. Atmos. Sci.*, **49,** 2564–2569.

Teillet, P. M., P. N. Slater, Y. Ding, R. P. Santer, R. D. Jackson, and M. S. Moran, 1990: Three methods for the absolute calibration of the NOAA AVHRR sensors in-flight. *Remote Sens. Environ.*, **31,** 105–120.

Thekaekara, M. P., R. Kruger, and C. H. Duncan, 1969: Solar irradiance measurements from a research aircraft. *Appl. Opt.*, **8,** 1713–1732.

Tsay, S., K. Stamnes, and K. Jayaweera, 1989: Radiative energy budget in the cloudy and hazy Arctic. *J. Atmos. Sci.*, **46,** 1002–1018.

Twomey, S., 1974: Pollution and the planetary albedo. *Atmos. Environ.*, **8,** 1251–1256.

——, 1991: Aerosols, clouds and radiation. *Atmos. Environ.*, **254,** 2435–2442.

——, and C. F. Bohren, 1980: Simple approximations for calculations of absorption in clouds. *J. Atmos. Sci.*, **37,** 2086–2094.

——, and T. Cocks, 1982: Spectral reflectance of clouds in the near-infrared: Comparison of measurements and calculations. *J. Meteor. Soc. Japan,* **60,** 583–592.

——, and ——, 1989: Remote sensing of cloud parameters from spectral reflectance measurements in the near-infrared. *Beitr. Phys. Atmos.*, **62,** 172–179.

——, H. Jacobowitz, and H. B. Howell, 1966: Matrix methods for multiple scattering problems. *J. Atmos. Sci.*, **23,** 101–108.